Journal of Materials Research and Technology 32 (2024) 2993–3003

Contents lists available at ScienceDirect

Journal of Materials Research and Technology

journal homepage: www.elsevier.com/locate/jmrt

Peak microhardness recovery via T6 heat treatment with extremely soft annealed Al7075 feedstock in additive friction stir deposition

Huan Ding [a,*], Uttam Bhandari [a], Pengcheng Zhu [b], Ehsan Bagheri [a], Saeid Zavari [a], Yehong Chen [a], Yang Mu [a], Yongqiang Wang [b], Shengmin Guo [a,**]

[a] Department of Mechanical and Industrial Engineering, Louisiana State University, Baton Rouge, LA, 70803, USA
[b] Los Alamos National Laboratory, Los Alamos, NM, 87545, USA

ARTICLE INFO

Keywords:
Additive friction stir deposition
Al7075
Annealing
Heat treatment
Peak microhardness recovery

ABSTRACT

With standard T6 heat treatments, precipitate-hardened alloys such as Al7075 and Al6061 fabricated using Additive Friction Stir Deposition (AFSD) method restore to noticeably different peak mechanical properties. Previous research observed similar results but did not provide a viable solution. This study proposes a new processing strategy, namely enhanced plastic deformation by subjecting the Al7075 feedstock to annealed softening treatments. Specifically, by annealing the standard T651-Al7075 feedstock and deposition substrate (179 HV), their Microhardness were first degraded to its lowest state (80 HV), which is called a Soft-to-Soft system. For the Soft-to-Soft system subjected to AFSD, after undergoing appropriate T6 heat treatment, the microhardness of the AFSD 7075 alloy was restored to its peak value (183.1 ± 1.8 HV). The results indicate that this softening strategy can effectively reduce the non-strengthening phase in the AFSD matrix, thereby increasing the strengthening phase (η' phase). This addresses the issue of traditional AFSD-prepared aluminum alloys being unable to achieve peak performance through T6 heat treatment.

1. Introduction

Aluminum alloy 7075 is known as a high-strength alloy. Its outstanding mechanical properties (high strength, low density, and high corrosion resistance) are widely recognized, and it is commonly used in the aerospace industry. The primary alloying elements in Al7075 are Al, Zn, Mg, and Cu. Its principal strengthening mechanism is the precipitation hardening mechanism, described by the theory of supersaturated solid solutions. The typical sequence of strengthening is Guinier-Preston (GP) zones (MgZn) – metastable η' - stable η ($MgZn_2$) [1]. Fe, Si, and Mn are impurities in the Al7075 alloy, prone to forming non-strengthening phases. Once formed, these non-strengthening phases will not re-dissolve into the matrix in the subsequent thermomechanical process [2]. Hence, the microstructure and mechanical properties of Al7075 can be significantly influenced by the manufacturing process and subsequent heat treatments, thus requiring the application of suitable aluminum alloy fabrication methods.

Distinguished from the traditional casting and forging of aluminum alloys, the emerging metal additive manufacturing (AM) technologies in recent years have provided new approaches for aluminum alloy fabrication. AM processes based on powder [3–5] and filament [6–9] feedstock materials can rapidly produce complex and precise alloy parts. Such as Aluminum [10–12], Inconel [13–16], and Copper alloy [17,18]. So far, numerous studies have been conducted concerning the microstructure, process parameters, and mechanical properties of AM aluminum alloys. However, due to the material property limitations of aluminum alloys, such as their high sensitivity to hot cracking and extremely poor weldability [19], utilizing the solidification-based additive manufacturing methods to achieve deposition of components without voids and hot cracks is challenging. Al7075 alloy has been reported [20,21] to display a significant amount of hot cracking and porosity defects when utilizing solidification-based AM methods, resulting in mechanical properties that are comparatively lower than standard values. Although researchers have improved the crack susceptibility of Al7075 by altering the alloy composition, the yield strength of samples [10], even after homogenization and artificial aging, remains significantly lower than that of the forged alloy Al 7075-T6. Therefore, solidification-based additive manufacturing processes have

* Corresponding author.
** Corresponding author.
E-mail address: hding3@lsu.edu (H. Ding).

https://doi.org/10.1016/j.jmrt.2024.08.132
Received 28 April 2024; Received in revised form 9 August 2024; Accepted 20 August 2024
Available online 22 August 2024

not been widely adopted for making 7075 aluminum parts.

Additive Friction Stir Deposition (AFSD) is a solid-state process that enables the fast and scalable additive manufacturing of a wide range of metals and metal matrix composites. It combines the principles of additive manufacturing with friction stir welding techniques. In simple terms, AFSD facilitates the deposition of material layer by layer, while seamlessly fusing these layers using the heat generated from friction. Unlike processes that involve melting and solidification stages, AFSD is a thermomechanical process where feedstock materials will not reach the melting temperature and has fewer requirements on the weldability. Internal defects, such as hot cracks and pores are effectively mitigated in parts manufactured by the AFSD method.

Currently, the primary commercial alloy used in AFSD is aluminum alloy. Such as the Al6061 [22–25], Al2050 [26], Al7075 [27–29]. Recent research has investigated the microstructure and mechanical properties of AFSD on different aluminum alloys. And researchers attempted to build a relationship between microstructure evolution and processing parameters. Moreover, as a novel Severe Plastic Deformation (SPD) technique, the predominant emphasis of microstructural studies about the AFSD of aluminum alloy is centered on understanding the mechanism underpinning grain refinement. Components fabricated through AFSD characteristically display 'wrought microstructures' characterized by ultra-fine equiaxed grains, as opposed to 'columnar grain microstructures' derived from solidification. This results in the achievement of the sought-after isotropic mechanical properties. According to previous research, there are scarce studies dedicated to the AFSD Al7075. Joey Griffiths et al. [30] assessed the hardness and microstructure of a repaired Al7075 plate in its as-deposited state. The plate, originally featuring a single hole, was filled using the AFSD process. Furthermore, Avery et al. [31] explored the fatigue behavior and resulting microstructure of an as-deposited monolithic AFSD Al7075 component. Lastly, Yoder et al. [27] performed a post heat-treatment study on AFSD produced Al7075 and found that the AFSD Al7075 alloy can only recover to 94% of the properties exhibited by the cast 7075-T6 alloy after T6 heat treatment.

There are still numerous challenges in the current research on AFSD. First, many researchers have found that it is difficult for AFSD samples to be restored to the high-strength state of the feedstock even through applying proper heat treatment [23,27,28,32,33]. Recently, there have been some studies achieving progress in performance improvement. Using T74, which has slightly lower strength than T6 strength, Hahn et al. [34] successfully prepared AFSD 7050 samples with comparable performance to forged 7050 alloy (tensile strength of 491 MPa) after the same T74 heat treatment. Liu et al. [35] reported research on the recovery of 7075 alloy performance. Although the final AFSD 7075 alloy achieved a high tensile strength of 560 MPa after T6 heat treatment, it was still lower than the T6 7075 feedstock material (577 MPa).

Most aluminum alloys, especially Al7075, belong to precipitation-hardened alloys. Grain refinement contributes minimally to strength enhancement, with the augmentation in strength primarily dominated by the formed precipitates. Researchers have already pointed out that the decline in the strength of such deposited alloys is due to the formation and growth of non-strengthening phases, inhibiting the formation of the primary strengthening phase. However, no existing studies have proposed appropriate solutions for AFSD Al7075. Although subsequent heat treatments can restore a portion of reduced mechanical properties, peak values cannot be attained. In addition, most reported AFSD Al7075 studies have a feeding rate of approximately 5–94 mm/min [23,36–39], which is quite slow for industrial applications. Considering the prospects of AFSD for large-scale production, elevating the feed rate is an imperative need.

In this study, for the first time, the potential solutions for the mentioned challenges above are reported. To start the discussion, we define the state of the standard material feedstock and substrate as Hard, and the annealed feedstock and substrate as Soft. Researchers normally focus on the standard feedstock and substrate in the AFSD process, the so-called Hard-to-Hard system. Almost no researchers have attempted to examine the printing performance and microstructure changes when the material transitions to a Soft-to-Soft system. To address the shortcomings of previous research, this study initially subjects commercial T651-7075 aluminum alloy to the annealing treatment, reducing the hardness to its minimum. Subsequently, the plastic deformation and precipitate behavior within the matrix of the as-deposited sample from the annealed 7075 rod and standard 7075 rod with a high feeding rate (~127 mm/min) are investigated in detail. The influence of the printed microstructure on the size and type of final precipitates is elucidated. Finally, by employing appropriate T6 heat treatment, the mechanical properties of the annealed deposited samples are restored to their peak. These findings provide an experimental basis and reference for the industrial application of the friction deposition process.

2. Materials and methods

A commercial L3 machine from MELD Manufacturing Corporation (USA) was used in this study. A thermocouple was implemented inside the substrate for temperature measurement. During the printing process, the substrate temperature was held at a range between 300 and 330 °C. In this study, the printing parameters range are as follows: rotation speed of 100–300 RPM, layer thickness of 1.5–3 mm, feeding rate of 100–127 mm/min, and traversing speed of 72–137 mm/min. The applied force is about 5000–6500 N.

The solid Standard Al7075 square Rods (SR) were cut by a water jet from the T651-Al7075 plates (purchased from OnlineMetals) with a size of 9.5 x 9.5 × 500 mm. Table 1 displays the nominal chemical composition of T651-Al7075 alloy. The Annealed Al7075 Rod (AR) is derived from the standard Al7075 rod annealed at 320 °C for 2h and then furnace cooled to room temperature. The SR was deposited on the original T651-Al7075 plate, and the AR was deposited on the annealed T651-Al7075 plate to form the Hard-to-Hard and Soft-to-Soft systems, respectively. To enable a smooth AFSD deposition, the surface of the feedstock rod is coated with a thin layer of graphite to act as a lubricant. T6 (Peak aging) and T73 (Over aging) Heat Treatments were performed following the standard ASTM-AMS2772H. Solution treatment was performed at 470 °C for 50 min or 2 h (determined according to the thickness of the sample), followed by water quenching. Finally, age treatment was conducted at 121 °C for 24 h or 110 and 170 °C aging for 7 h, respectively, followed by natural cooling in the furnace.

The samples, once deposited, were subsequently sectioned using wire Electrical Discharge Machining (EDM). Both the top surface, which is perpendicular to the feeding direction, and the cross-section, which is parallel to the feeding direction, were sectioned. These were the designated surfaces for analyzing the microstructure, phase structure, composition distribution, and hardness.

All sample surfaces were mechanically roughly refined using SiC sandpapers, progressing in grit from 400, 600, 800, and 1000. Afterward, they were polished with DIAMAT polycrystalline diamond polishing pads (6 μm, 3 μm, and 1 μm) to attain a mirror surface. The final polishing process was performed on a vibratory polisher (Pace Technologies GIGA Vibratory Polisher) for 5-h in a pulse mode with 35 nm silica suspension.

X-ray diffraction (XRD) examination was performed on a PANalytical Empyrean system with Cu Kα radiation. Symmetric θ/2θ scans were conducted in the angular range of 5–90° 2θ, with a scanning step size of 0.013°. Scanning Electron Microscopy (SEM) and Energy Dispersive Spectroscopy (EDS) were performed on the ThermoFisher Helio G5 Xe PFIB/SEM system. Electron Backscatter Diffraction (EBSD) mapping was performed at 20 kV and 1.6 nA with an EBSD detector on the same PFIB/SEM system. Grain size was also calculated from the EBSD data as the equivalent circular diameter. ThermoFisher Titan 80–300 Transmission Electron Microscopy (TEM) with full XEDS was used to observe the nano-scale precipitates. Microhardness tests were performed on the specimens using a CM-802 AT microhardness tester, with a test load of

Table 1
Elements content of the commercial T651-Al7075.

Al	Zn	Mg	Cu	Fe	Cr	Mn	Si	Ti	Zr + Ti
Balance	5.1–6.1	2.1–2.9	1.2–2	0.5	0.2–0.3	0.3	0.4	0.2	0.25

200 gf and a dwell time of 15 s.

3. Results

3.1. Microstructure and microhardness evolution with annealed condition

Fig. 1 shows the microhardness of the SR and AR feedstock rods. The average hardness value is 179.3 ± 3.2 HV and 80.1 ± 2.1 HV for SR and AR, respectively. After the annealing process, the rod becomes extremely soft.

Annealing scarcely leads to grain coarsening [40], the grain growth process is constrained due to the presence of precipitate and dispersoid particles in the grain boundary, the so-called Zener Pinning effect. It was verified by the EBSD results as shown in Fig. 1. The hardness variation in the annealed 7075 rod therefore should originate from the evolution of the precipitates in the matrix. Many studies have already compared various strengthening mechanisms in Al alloys, concluding that the primary strength contribution in Al alloys arises from incoherent strengthening phases, here in 7075 alloys is the incoherent η′ phase. The contribution of the presence of incoherent precipitates in Aluminum alloy after T6 heat treatment (Orowan dislocation shearing mechanisms) is nearly 60% [41].

To further explore the phase transformation evolution within the matrix, we utilized the Focused Ion Beam (FIB) to thin a random area of the rod material (20 x 15 × 2 μm) down to 100 nm. The changes in the precipitates within the matrix were then observed using the STEM mode. EDS mapping was also employed to investigate the second phase in the matrix of both the standard 7075 rod and the annealed rod. Based on the STEM HADDF images in Fig. 2(a) and (b), the most noticeable changes in the precipitates within the matrix are alterations in shape and size. In the SR, predominantly plate-like precipitates and extremely fine spherical particles precipitate, whereas in the AR, coarsened plate-like precipitates emerge. Considerable research [42,43] has shown that the type of precipitates in T6-7075 can be approximately determined by their size and shape. And a variety of precipitate types in 7075 have been extensively reported. Therefore, in the current sample, the precipitates are divided into the main strengthening phase of semi-coherent η′ phase (~0–10 nm) and the needle and plate-like incoherent η phase (~50–150 nm).

According to the precipitation mechanism of Al7075 alloy, after annealing at 320 °C, the semi-coherent η′ phase will transform into the more stable η phase. This results in a significant decrease in hardness and an improvement in ductility. EDS mapping of the feedstock with and without annealed condition is also shown in Fig. 2. In the SR, the coarse phase is primarily composed of magnesium and zinc elements, with only trace amounts of copper. These coarse grains, defined as the η phase due to their size exceeding 50 nm, contain finer phases that are beyond the scanning precision of EDS for elemental analysis. However, based on the characteristics of precipitate phases mentioned earlier, these finer phases are identified as η'. In the AR, the ultra-fine precipitates disappear, nearly all transforming into coarse precipitates, and the transformed η phase contains a significant amount of Cu elements. The dimensions of η phases, measured using ImageJ software, ranged from 50 nm to 150 nm in width. This aligns with the size of the η phases shown in previous studies [44].

3.2. After deposition

To assess the strength variation of the printed samples, microhardness tests were initially conducted on the samples. Fig. 3(a) illustrates the schematic diagram of AFSD printing for hard-on-hard and soft-on-soft systems, simultaneously indicating the regions for cross-section area sampling. Fig. 3(b) shows the hardness measurement area and its direction on the cross-section, encompassing a total of 27 points from the top to the substrate. Fig. 3(c) displays the measured hardness values. The average microhardness of SR_AFSD and AR_AFSD is 81.3 ± 3.2 HV

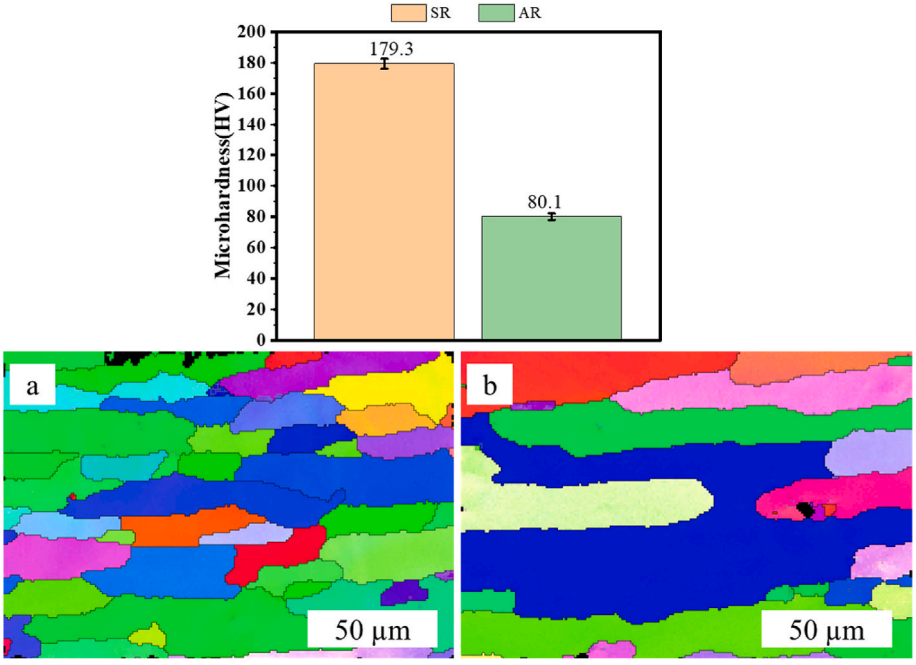

Fig. 1. Microhardness of the SR and AR feedstock and EBSD image for (a) SR (b) AR.

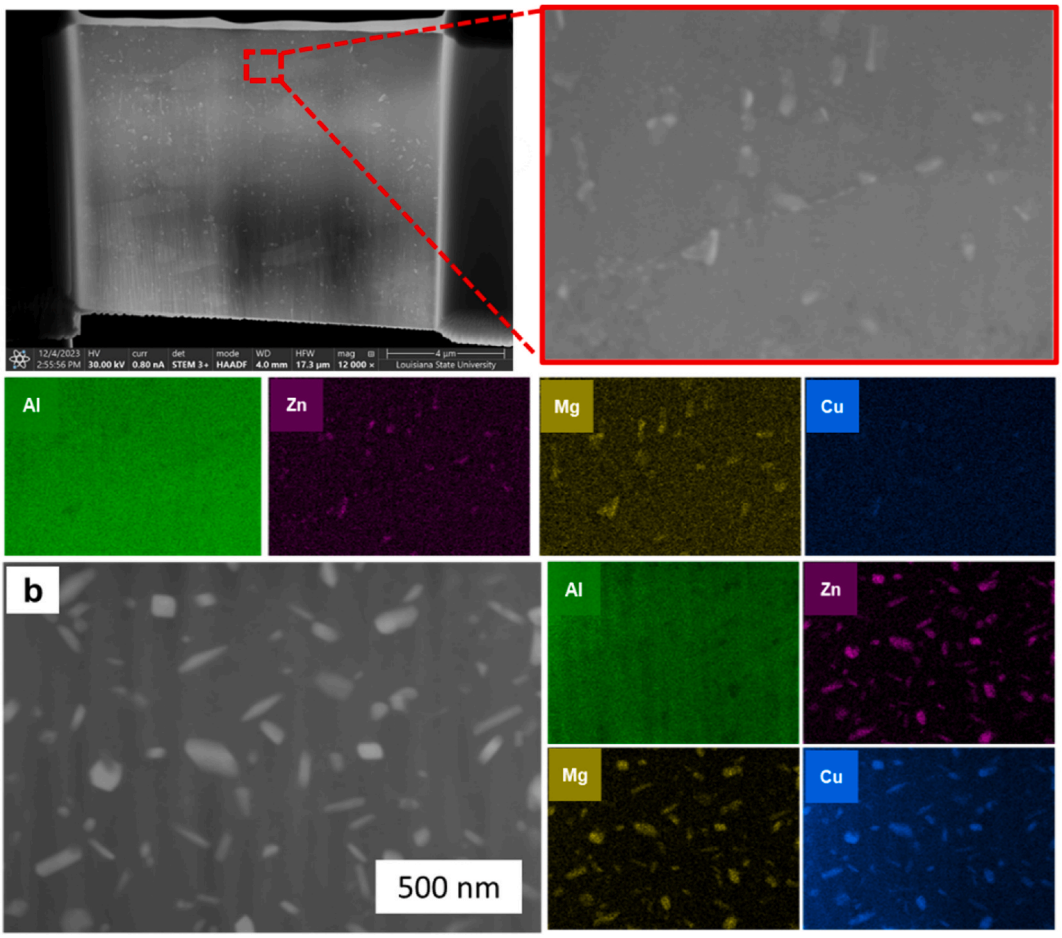

Fig. 2. STEM and EDS mapping for the (a) Standard 7075 rod (SR) (b) Annealed 7075 rod (AR).

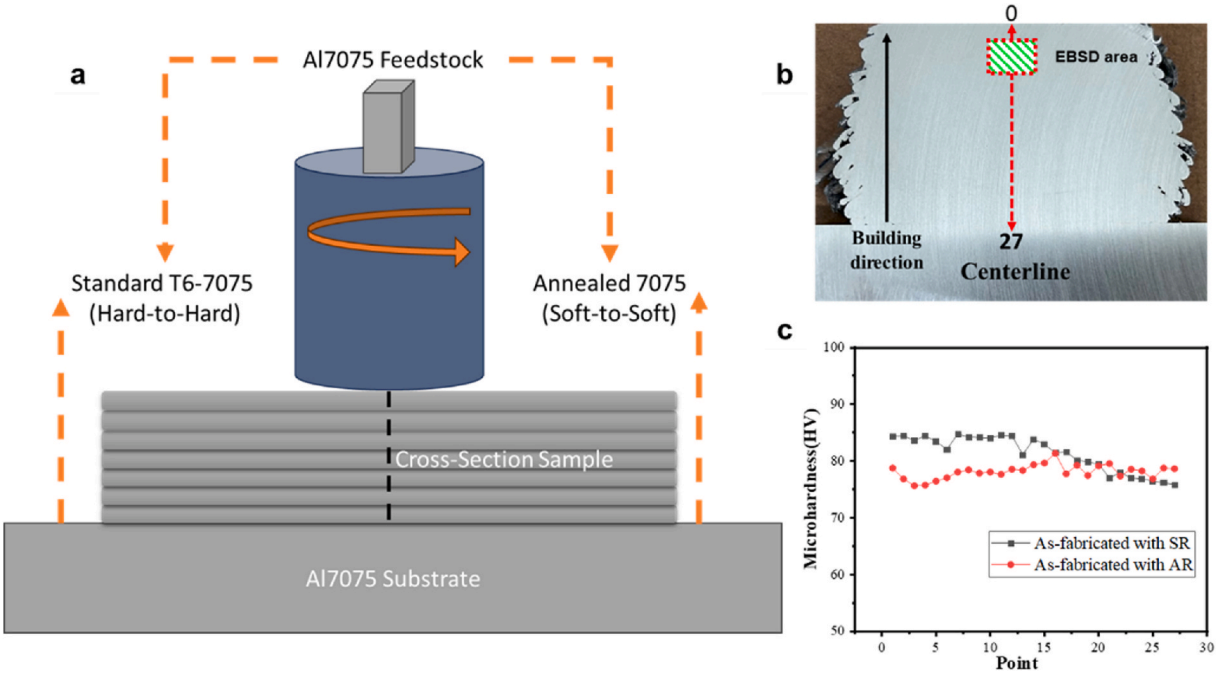

Fig. 3. (a) AFSD schematic diagram (b)AFSD cross-section area and hardness testing line (c) Microhardness of the AFSD samples.

and 78.1 ± 1.3 HV, respectively. It is noteworthy that the hardness values of AR_AFSD exhibit minimal variation from the top to the bottom, with the range between the maximum and minimum values being approximately 6%. Conversely, the hardness values of SR_AFSD demonstrate a declining trend from the top to the bottom, with a variation of about 12%. The changes in hardness indicate that annealed 7075 rods exhibit greater advantages in terms of overall uniformity in microstructure and properties after the AFSD process.

To investigate the grain evolution of AFSD samples, EBSD was utilized to examine the grain information of the samples. Fig. 4 presents the Inverse Pore Figure (IPF) and Grain Reference Orientation Deviation (GROD) of the SR_AFSD and AR_AFSD. The EBSD detection area is located in the centerline top region of the AFSD sample cross-section.

Based on the IPF map, grain refinement in the AFSD samples can be distinctly observed. The average grain size of the SR_AFSD and AR_AFSD based on the area-weight mean was 4.90 ± 1.6 μm and 5.6 ± 1.8 μm while grain size of the 7075 feedstock was ~100 μm [22]. Interestingly, SR_AFSD presents relatively standard equiaxed grains, while AR_AFSD exhibits elongated equiaxed grains. Moreover, it can be noted that grains with high-angle grain boundaries predominate in SR_AFSD, accounting for 88.3%, whereas AR_AFSD sees a rise in the proportion of grains with low-angle grain boundaries, indicating the addition of more sub-grain boundaries in the matrix. Both sub-boundaries and low-angle interfaces can be considered accumulations of dislocations, roughly representing the dislocation density. This point is also validated in the GROD (Grain Reference Orientation Deviation) map. The level of plastic deformation is closely related to GROD. The GROD angle provides a measure to characterize the angular deviation between points within a single grain and the average orientation of the given grain. Overall, the dislocation density and degree of deformation are directly proportional to the maximum GROD angle value. The average GROD angle of the SR_AFSD and AR_AFSD was 1.20° and 1.75° respectively. In AR_AFSD, the highest GROD angle can reach 11.1°, while in SR_AFSD, the highest GROD angle is only 7.0°. This indicates that the rod, after annealing and softening, undergoes more plastic deformation and dislocation accumulation when processed through AFSD.

To further explore the relationship between performance and microstructure, EDS and XRD were employed to analyze the precipitates in the matrix. Fig. 5 (a) and (b) display the distribution of precipitates and elemental information in SR_AFSD and AR_AFSD. Overall, the average size of precipitates in SR_AFSD is smaller than that in AR_AFSD (Red rectangular). This is also reflected in the distribution maps of elements such as Zn, Mg, and Cu. However, a substantial amount of secondary phases related to impurity elements (Fe, Si) have emerged in SR_AFSD. Based on the composition of the impurity phases, some phases cannot re-dissolve into the matrix, especially Mg_2Si. This also explains why AFSD samples cannot be restored to optimal performance through heat treatment. These non-strengthening phases will reduce the strengthening solute elements in the matrix, such as Mg, Cu, Zn, etc., resulting in a decreased mass fraction of the ultimately formed strengthening phases (η' $MgZn_2$). The strengthening mechanism of the Al7075 alloy is primarily controlled by precipitation strengthening, facilitated by either Orowan bypass mechanism or dislocation shear mechanisms. In the 7075 alloy, these non-strengthening phases typically exist incoherently with the matrix, and a large amount of non-strengthening phases can lead to a reduction in the semi-coherent strengthening η' phase during the following aging process. This can trigger the Orowan bypass mechanism [45], resulting in a relatively small increase in microhardness. An increase in the strengthening η' within the matrix promotes the dislocation shear mechanism, thereby significantly enhancing the microhardness of the matrix. After the feedstock rod is annealed, it can be observed in AR_AFSD that the number of non-strengthening phases, caused by impurity elements, is significantly reduced.

Fig. 6 displays the XRD diffraction spectra of the two AFSD samples. The results also support the viewpoint that the precipitate phases/non-strengthening phases in the matrix decrease with the annealing of the rod. First, compared to the SR_AFSD sample, the peaks in AR_AFSD shift to the left. According to Bragg's Law, a decrease in the 2θ angle implies an increase in lattice spacing, indicating an increase in the solute fraction. Specifically, the 2θ angle of (111) diffraction peaks of SR_AFSD and AR_AFSD are 38.50° and 38.42°, respectively. The calculated lattice parameter for AR_AFSD (0.4054 nm) is 0.22% larger than that for SR_AFSD (0.4045 nm), using the mean free path λ = 0.154 nm. This

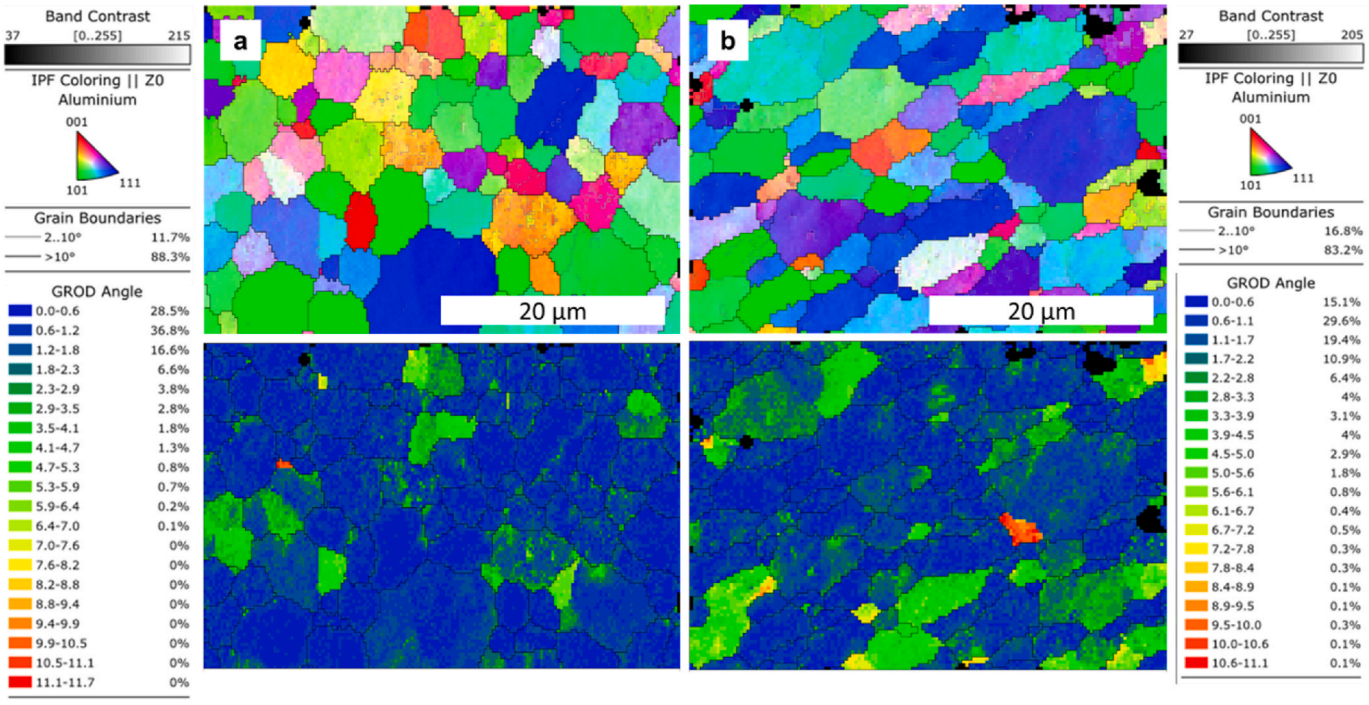

Fig. 4. Ebsd IPF and GROD for (a) SR_AFSD (b) AR_AFSD.

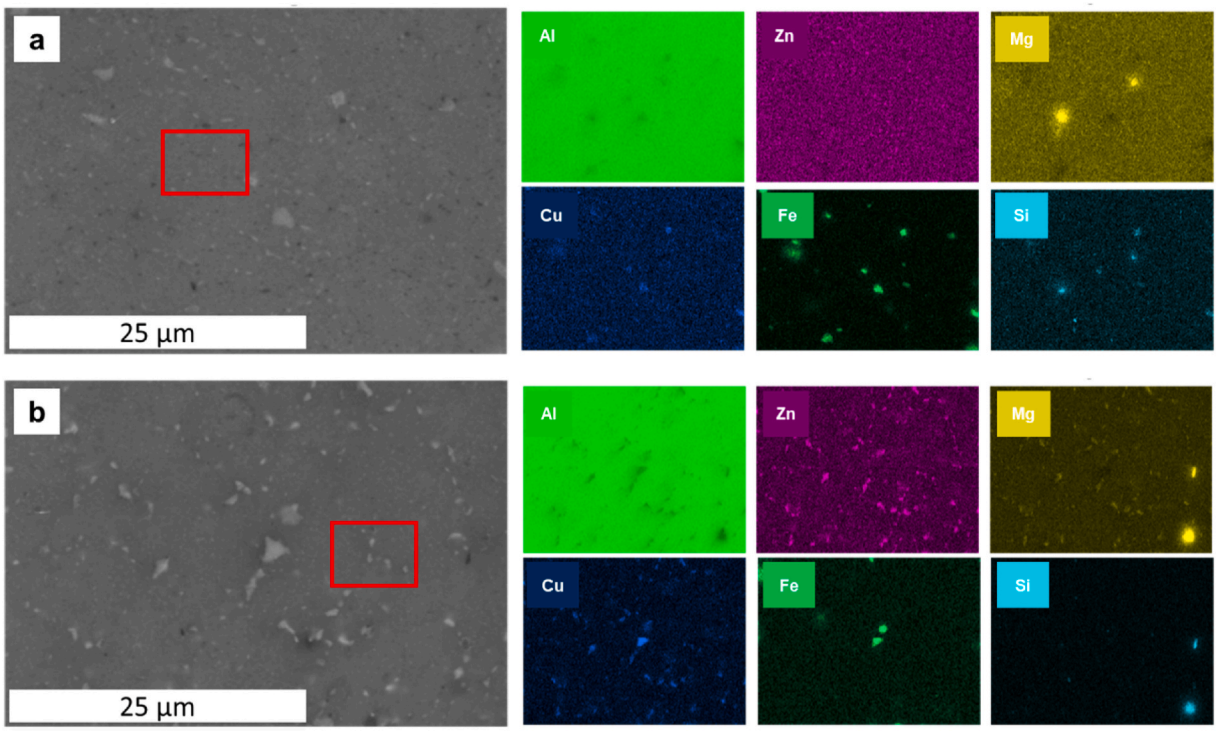

Fig. 5. EDS mapping of (a) SR_AFSD (b) AR_AFSD.

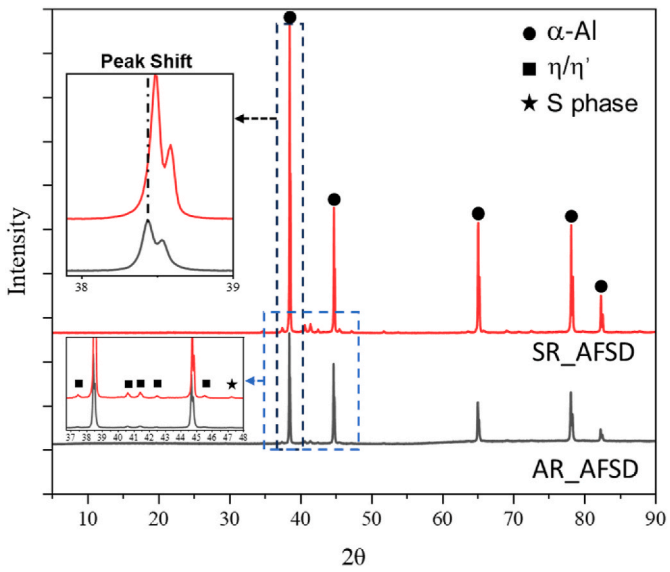

Fig. 6. XRD for AFSD sample.

indicates that AR can inhibit the migration of solute atoms from the α-Al phase lattice to form precipitates, thereby increasing the lattice parameters of the aluminum matrix. Moreover, the presence of the S phase (Al–Cu–Mg) was slightly detected in SR_AFSD, which is absent in AR_AFSD.

3.3. Hardness evolution after peak aging and over aging

To evaluate the recovery of the properties of the AFSD samples, both types of samples were subjected to T6 and T73 heat treatment according to ASTM standards (ASM2772H). TX-1 means the solution time is 50 min while TX-2 is 2 h. Their hardness is displayed in Fig. 7. After T6-1 heat treatment, the average hardness of SR_AFSD_T6 and AR_AFSD_T6 is 172.8 ± 10.3 HV and 183.1 ± 1.8 HV, respectively. The AR_AFSD_T6 sample even surpassed the raw feedstock hardness of T651-7075 (179HV). It is noteworthy that several regions of low hardness (155HV) were observed in the SR_AFSD_T6 sample, which may be attributed to incomplete dissolution of precipitates. With a further increase in solution treatment time to 2 h (T6-2), these unstable regions disappear, and the hardness remains almost unchanged. The evolution of hardness maintains a similar trend during over-aging as well. After T73 heat treatment, the average hardness for SR and AR samples is 162.5 ± 1.7 HV and 170.1 ± 1.2 HV, respectively. It is well known that overaging, i.e., the T73 state, can greatly enhance stress corrosion cracking (SCC) resistance. Unfortunately, compared to the T6 state, the microhardness is usually reduced by 10%–15%. However, the microhardness of the AR_AFSD_T73 sample only decreased by 5% compared to the T6 peak sample, which is undoubtedly a performance improvement.

After undergoing standard T6 heat treatment, the precipitates in the sample should transform into ultrafine nanoscale precipitates [46]. SEM-EDS was first utilized to capture the morphology of the precipitates, and Fig. 8 shows the EDS mapping results of the T6-7075 feedstock rod and the heat-treated samples. EDS maps illustrate the different precipitates in the three samples, along with a quantitative analysis of the elemental composition. It is evident that an increase in non-strengthening phases is the main reason why AFSD 7075 cannot regain peak microhardness through T6 heat treatment. Both the standard T6-7075 feedstock and the AR_AFSD_T6 sample exhibit fewer non-strengthening phases. The difference lies in the fact that in the T6-7075 feedstock, the non-strengthening phases are mainly related to Mg, Cu, and Si, whereas in the AFSD sample, the non-reinforcing phases are primarily related to Mg, Fe, and Si. By analyzing the overlapping regions, the non-strengthening phases are identified as Mg_2Si, Al_2Cu, and the complex phase related to Fe and Si.

Fig. 9 shows the XRD spectra of SR_AFSD_T6 and AR_AFSD_T6. Due to the nano size of the secondary phase, the intensity of the secondary phase peak on the XRD spectra is extremely weak. An attempt was made to quantitatively analyze the Al matrix and η′ strengthening phase using HighScore software. The results indicate that compared to the

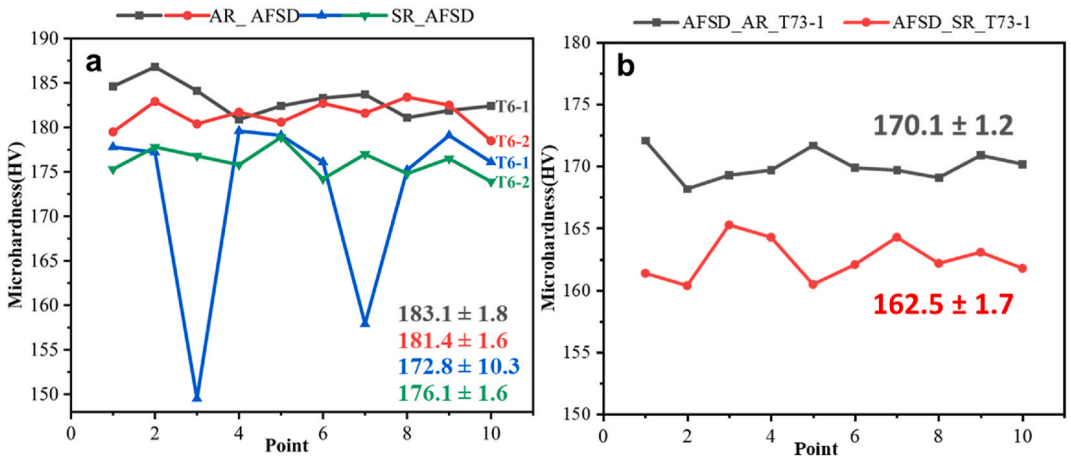

Fig. 7. Microhardness for the AFSD sample after different heat treatment conditions (a) T6 (b) T73.

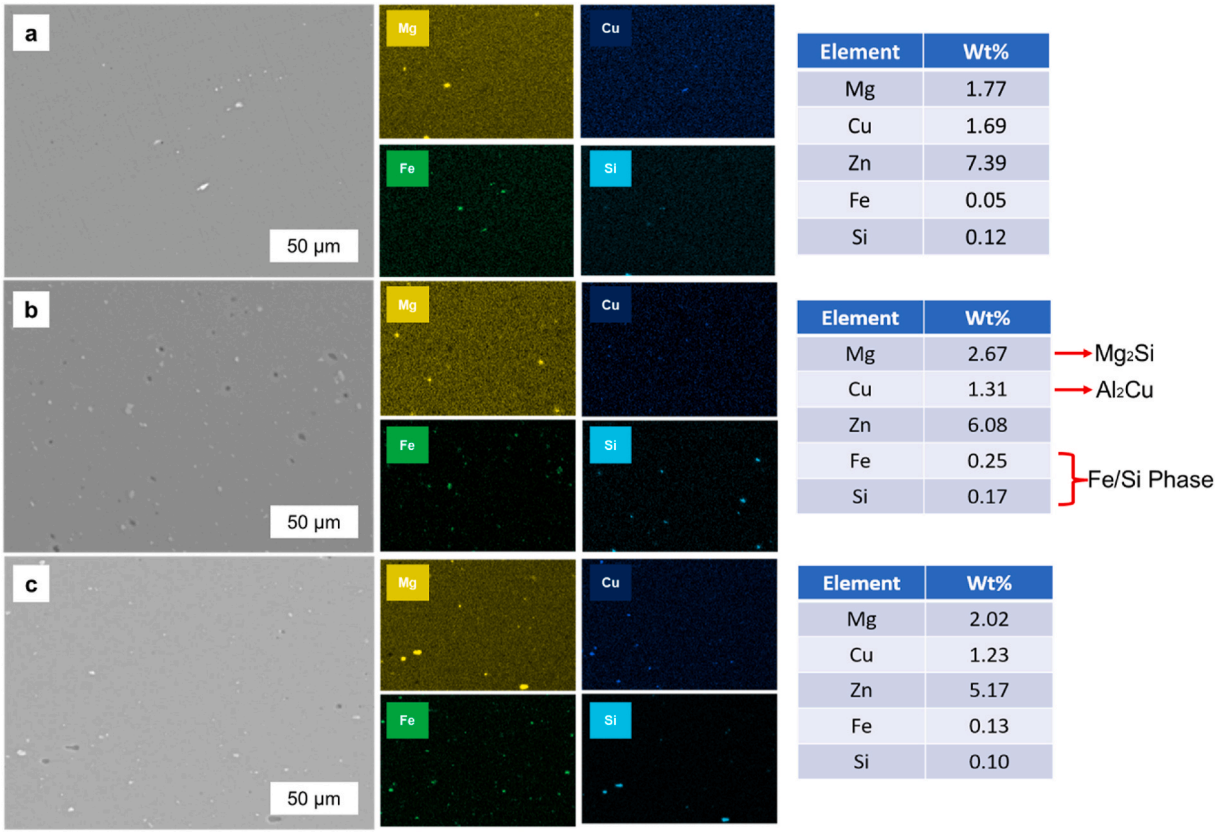

Fig. 8. EDS mapping of (a) T6_Feedstock rod (b) SR_AFSD_T6 (c) AR_AFSD_T6.

SR_AFSD_T6 sample, the content of the η′ strengthening phase in AR_AFSD_T6 increased from 1.9% to 2.1%. Considering the variation in hardness, we believe that this numerical range is reasonable.

To further investigate the shape and size of the precipitates in the SR_AFSD_T6 and AR_AFSD_T6 samples, TEM-EDS was adopted. As shown in Figs. 10 and 11, the white dashed regions in the TEM images depict the typical grain morphology of the samples. They suggest that even after high-temperature treatment, the grain size and shape of the AFSD sample did not undergo significant changes. The SR_AFSD_T6 sample mainly consists of equiaxed-like grains, whereas the AR_AFSD_T6 sample is dominated by elongated equiaxed grains. Fig. 10 illustrates STEM images of the distribution of precipitates in SR_AFSD_T6 at low and high magnification. It can be observed in Fig. 10 (a) that these precipitates exhibit non-uniform distribution and vary significantly in size and shape, ranging from 30 nm to 800 nm and rod-like to plate-like. With further increase in magnification, extremely fine second-phase particles (less than 10 nm) distributed within the grains can be observed, primarily composed of Mg and Zn. Numerous reports [27,36,42,44,47] have shown that these nanoscale MgZn particles are η′ phase. It is noteworthy that coarsened MgZn particles were observed at the grain boundaries, with sizes around 20–50 nm. It can be identified as the η phase. Additionally, a large size type of S phase (Cu related) and E phase (Cr related) were also detected in the matrix. In contrast to the SR sample, the distribution of precipitates in the AR_AFSD_T6 sample is more uniform, with shapes tending toward spherical, as shown in Fig. 11 (a). Extremely fine and uniformly distributed η′ particles (approximately

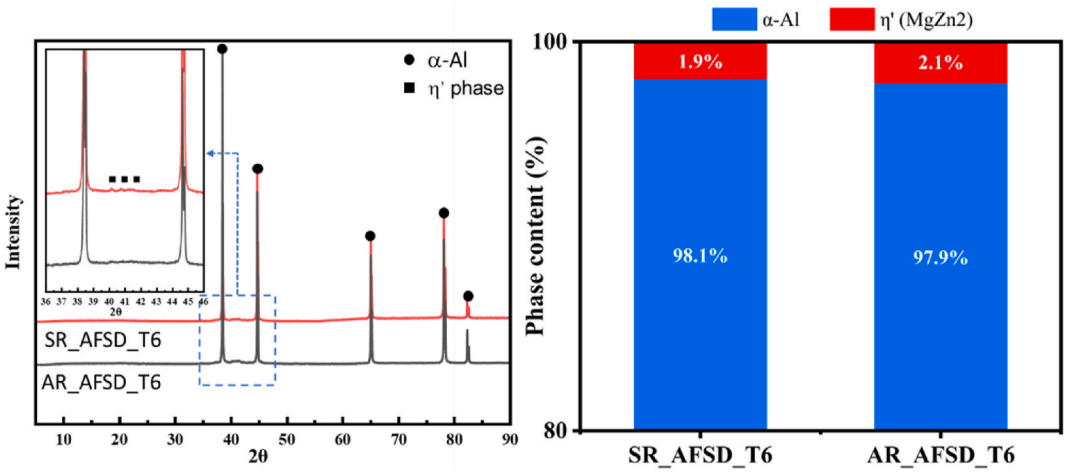

Fig. 9. XRD pattern for the Post heat treated AFSD sample and the phase content.

4–5 nm) were also present within the grains. However, unlike SR samples, no coarsened MgZn particles were detected at the grain boundaries. Overall, the types of precipitates present in both AFSD_T6 samples are nearly identical. The hardness difference is influenced by the uniformity of precipitates in SR and AR samples and the presence or absence of coarsened MgZn particles at the grain boundaries. The presence of less non-strengthening phase density of precipitates in AR_AFSD_T6 compared to SR AFSD_T6 indicates a higher degree of strengthening within the material due to impeding dislocation by precipitations. The non-uniform nucleation issues caused by impurity elements (Fe and Si) or dislocations necessitate further investigation in the future.

4. Discussion

From the above experimental results, it can be observed that the annealed 7075 rods altered the precipitation behavior during the AFSD process. The primary reason lies in the significant difference between the precipitates in the annealed 7075 rod and those in the standard 7075 rod. For the AR 7075, the strengthening η′ phase in the matrix has almost completely disappeared. According to related reports in the literature [40,48], η′ phase may transform into the finer non-coherent η phase after annealing. This explains why extremely fine precipitates were only found in the SR and not in the AR. At the same time, the transition from semi-coherent to non-coherent phases also causes the precipitate particles to lose their hardening effect due to their incoherence with the matrix. It is inferred that before AFSD, the primary phase is η′ strengthening phase in SR and η phase in AR Concurrently, the microhardness decreases from 179 HV for SR to 80 HV for AR.

During the AFSD process, the rod undergoes high strain, introducing high-density dislocations due to intense plastic deformation, and ultimately obtaining refined grains under the CDRX mechanism [22]. For SR 7075, precipitation behavior can be divided into three stages. In the first stage, the semi-coherent η′ phase is uniformly distributed in the rod. When the SR undergoes severe plastic deformation, η′ phase can be fragmented to an extremely small size or even re-dissolved into the matrix. In the second stage, at this point, the η′ phase in the matrix begins to transform into η phase, accompanied by the precipitation of other impurity elements (Fe, Si) secondary phases. Since the high dislocation density and high vacancy concentration introduced by AFSD, nucleation sites for precipitate secondary phases are provided. This can be explained by the accelerated diffusion of alloy elements within the dislocation cores and the increased space for alloy atoms in the expanded regions around the dislocations. In the final stage, based on the thermal cycle history during the AFSD process, the η phase will gradually coarsen. For AR 7075, since the η′ phase does not exist in the rod, there is no phase transition from η′ phase to η phase during the AFSD process. After undergoing a brief grain rearrangement, the η phase directly begins to coarsen. Given the absence of the phase transition stage of precipitation behavior in AR and combined with the reduction in the quantity of Fe and Si-related non-strengthening phases in Fig. 5 (b), we can reasonably infer that this impurity phase might mainly form during the phase transition (η′ phase to η phase) process. Consequently, the growth of the η phase has the highest priority in the AFSD process. It will inhibit the formation and growth of non-strengthening phases. This precipitation behavior is consistent with the EDS mapping results. Due to undergoing a relatively shorter precipitation growth stage, the primary precipitates in SR_AFSD are smaller in size than those in AR_AFSD. However, there are more non-strengthening phases present in SR_AFSD.

The hardness of the AR_AFSD sample is slightly lower than that of the SR_AFSD sample, a phenomenon also observed by other researchers [27]. The authors also attempted direct aging of the SR_AFSD and AR_AFSD 7075 samples, with the maximum hardness only recovering to about 150 HV. This indicates that after the original rod undergoes AFSD processing, some non-strengthening phases are generated. This leads to a reduction of strengthening solute elements in the Al matrix and alters the kinetics of precipitate precipitation during subsequent heat treatment, thereby making it impossible to recover peak microhardness through aging alone. This study further observed that the high solubility of the AR_AFSD matrix resulted in a lower mass fraction of non-strengthening phases (Fe and Si related) that are insoluble in the matrix. Therefore, after undergoing the same T6 heat treatment, AR_AFSD_T6 almost recovered to peak hardness. Conversely, SR_AFSD_T6 exhibited lower hardness due to the presence of some harmful phases in SR_AFSD that do not dissolve back into the matrix, weakening the precipitation of strengthening solute elements.

5. Conclusions

In this study, we report for the first time the potential advantages of applying pre-annealed rod material in the AFSD method. Al7075 AFSD samples were fabricated utilizing two distinct states of Al7075, referred to as the Hard-to-Hard system (T6 Al7075 rod and substrate) and the Soft-to-Soft system (Annealed Al7075 rod and substrate). The following conclusion can be reached.

(1) The annealed rod demonstrated extremely low strength and, under the same AFSD deposition parameters, underwent more plastic deformation.
(2) The AFSD sample deposited from the annealed rod exhibited a reduced fraction of non-strengthening phases that are insoluble in the matrix, allowing it to recover peak microhardness through subsequent appropriate T6 heat treatment processes.

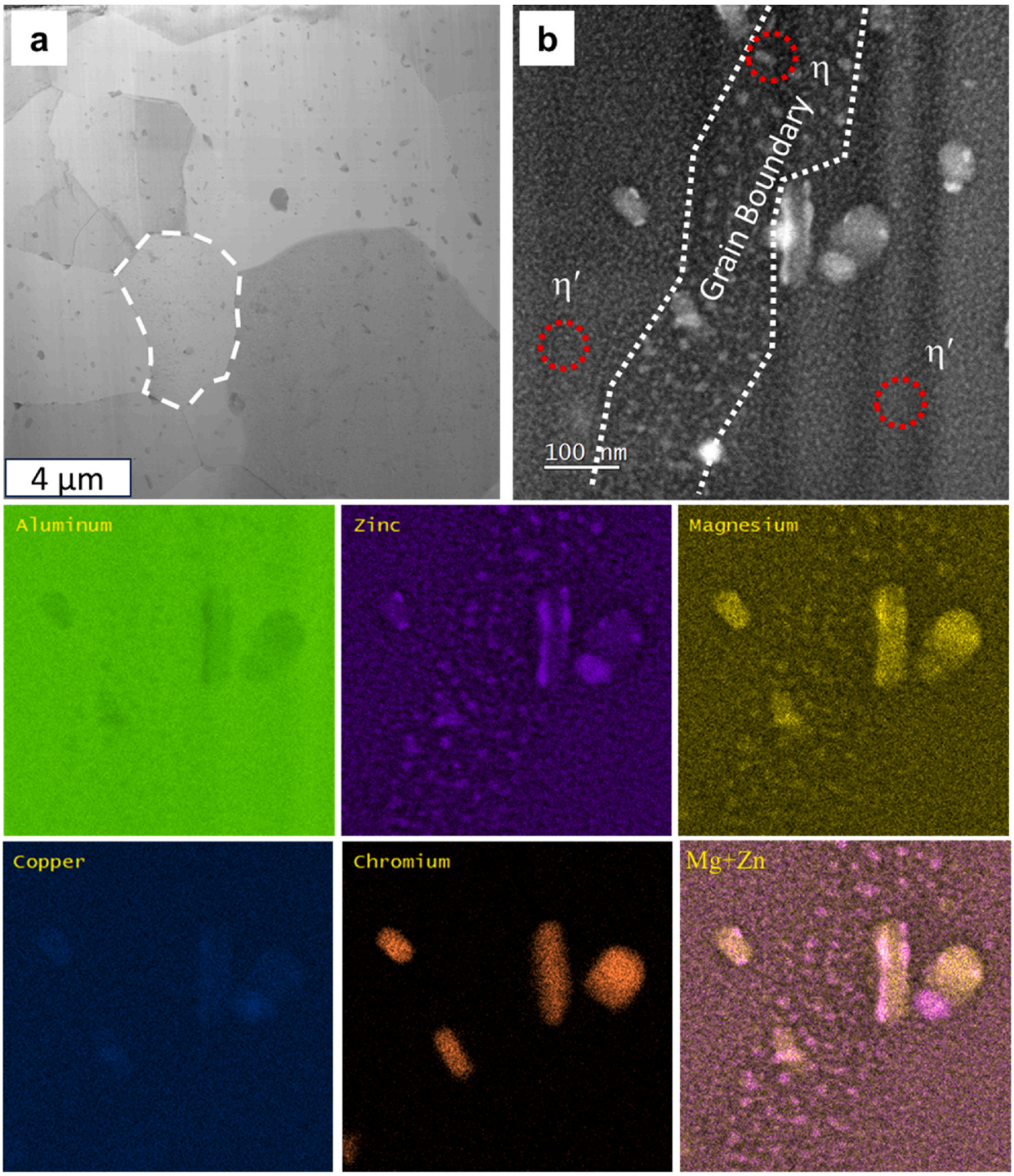

Fig. 10. (a) Bright-field STEM image and (b) HAADF image near the grain boundary with STEM-EDS for SR_AFSD_T6.

(3) After T73 heat treatment, the microhardness of AR_AFSD samples decreased by only 5% compared to SR_AFSD samples. This is also a potential application direction, aiming to maintain high strength while improving the stress corrosion cracking resistance of 7075 alloys.
(4) Pre-annealing the rod material not only enhances ductility but also reduces energy input and prevents mechanical deformation of the substrate. This significantly lowers the difficulty of AFSD processing.

Funding

This work is supported by the US National Science Foundation under grant number OIA-1946231 and the Louisiana Board of Regents for the Louisiana Materials Design Alliance (LAMDA). SG is partically supported by the industry members of the Center for Innovations in Structural Integrity Assurance (CISIA) under the US National Science Foundation Award number 2052810.

Data availability

Data will be made available on request.

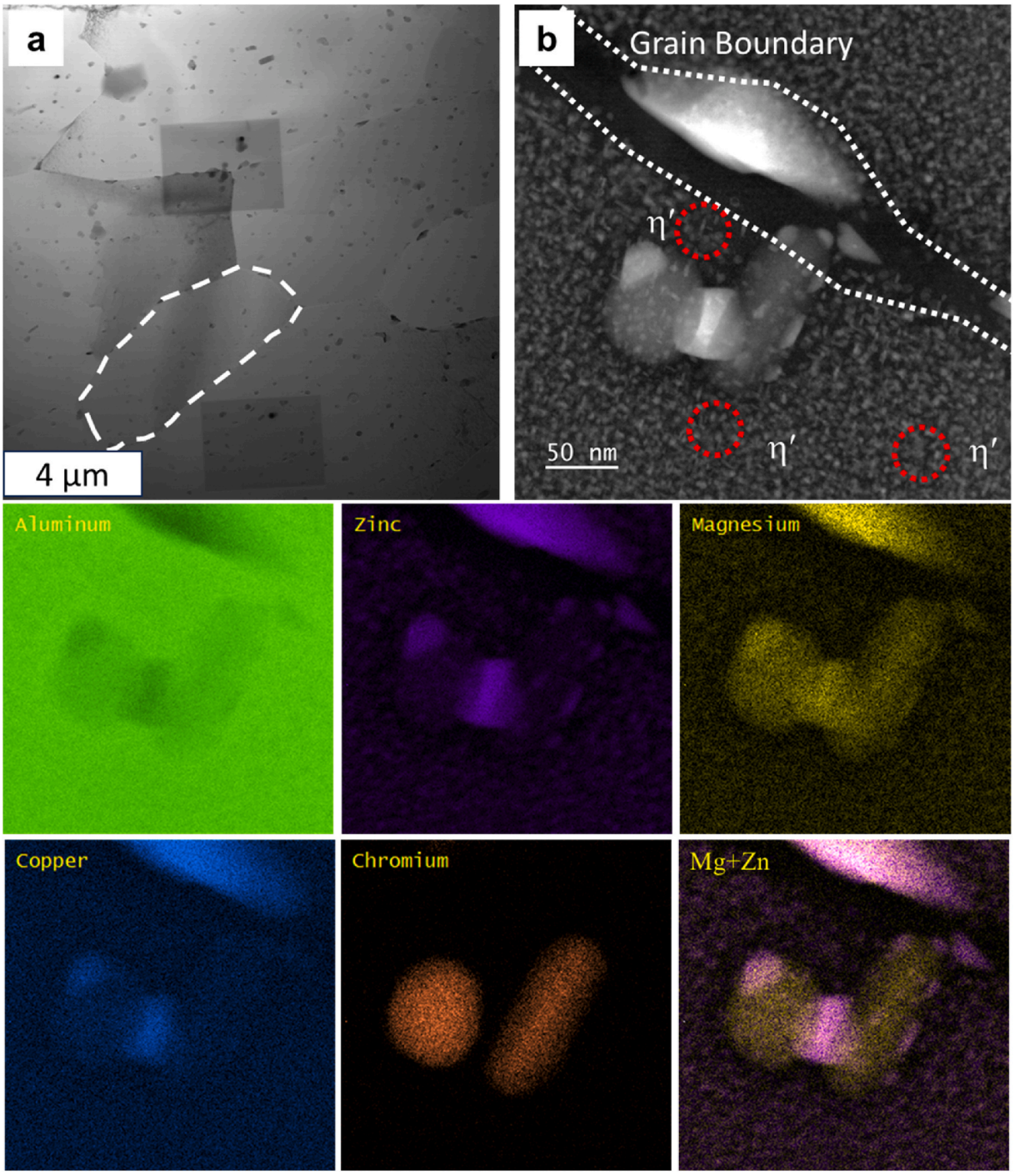

Fig. 11. (a) Bright-field STEM image and (b) HAADF image near the grain boundary with STEM-EDS for AR_AFSD_T6.

CRediT authorship contribution statement

Huan Ding: Conceptualization, Methodology, Investigation, Writing – original draft, Writing – review & editing. **Uttam Bhandari:** Writing – review & editing. **Pengcheng Zhu:** Investigation, Writing – review & editing. **Ehsan Bagheri:** Investigation. **Saeid Zavari:** Investigation. **Yehong Chen:** Investigation. **Yang Mu:** Investigation. **Yongqiang Wang:** Writing – review & editing. **Shengmin Guo:** Writing – review & editing, Funding acquisition.

Declaration of competing interest

The authors declare that they have no known competing financial interests or personal relationships that could have appeared to influence the work reported in this paper.

References

[1] Totten GE, MacKenzie DS. Handbook of aluminum: vol. 1: physical metallurgy and processes. CRC press; 2003.
[2] Singh SS, Schwartzstein C, Williams JJ, Xiao X, De Carlo F, Chawla N. 3D microstructural characterization and mechanical properties of constituent particles in Al 7075 alloys using X-ray synchrotron tomography and nanoindentation. J Alloys Compd 2014;602:163–74.

[3] Cao Y, Wei H, Yang T, Liu T, Liao W. Printability assessment with porosity and solidification cracking susceptibilities for a high strength aluminum alloy during laser powder bed fusion. Addit Manuf 2021;46:102103.
[4] Romano J, Ladani L, Razmi J, Sadowski M. Temperature distribution and melt geometry in laser and electron-beam melting processes–A comparison among common materials. Addit Manuf 2015;8:1–11.
[5] Kimura T, Nakamoto T, Ozaki T, Miki T. Microstructures and mechanical properties of aluminum-transition metal binary alloys (Al-Fe, Al-Mn, and Al-Cr) processed by laser powder bed fusion. J Alloys Compd 2021;872:159680.
[6] Ding H, Zeng C, Raush J, Momeni K, Guo S. Developing fused deposition modeling additive manufacturing processing strategies for aluminum alloy 7075: sample preparation and metallographic characterization. Materials 2022;15.
[7] Messimer SL, Patterson AE, Muna N, Deshpande AP, Rocha Pereira T. Characterization and processing behavior of heated aluminum-polycarbonate composite build plates for the FDM additive manufacturing process. Journal of Manufacturing and Materials Processing 2018;2:12.
[8] Momeni K, Neshani S, Uba C, Ding H, Raush J, Guo S. Engineering the surface melt for in-space manufacturing of aluminum parts. J Mater Eng Perform 2022;31:6092–100.
[9] Ghadimi H, Jirandehi AP, Nemati S, Ding H, Garbie A, Raush J, Zeng C, Guo S. Effects of printing layer orientation on the high-frequency bending-fatigue life and tensile strength of additively manufactured 17-4 PH stainless steel. Materials 2023;16:469.
[10] Martin JH, Yahata BD, Hundley JM, Mayer JA, Schaedler TA, Pollock TM. 3D printing of high-strength aluminium alloys. Nature 2017;549:365–9.
[11] Wang J, Gao J, Yang H, Yang F, Wen T, Liu Z, Zhang L, Ji S. High-strength Al–5Mg2Si–2Mg–2Fe alloy with extremely high Fe content for green industrial application through additive manufacturing. Virtual Phys Prototyp 2023;18:e2235587.
[12] Cordova L, Bor T, de Smit M, Carmignato S, Campos M, Tinga T. Effects of powder reuse on the microstructure and mechanical behaviour of Al–Mg–Sc–Zr alloy processed by laser powder bed fusion (LPBF). Addit Manuf 2020;36:101625.
[13] Kumar SP, Elangovan S, Mohanraj R, Ramakrishna J. A review on properties of Inconel 625 and Inconel 718 fabricated using direct energy deposition. Mater Today Proc 2021;46:7892–906.
[14] Zhang B, Ding H, Meng AC, Nemati S, Guo S, Meng WJ. Crack reduction in Inconel 939 with Si addition processed by laser powder bed fusion additive manufacturing. Addit Manuf 2023;72.
[15] Ding H, Emanet S, Chen Y, Guo S. The potential benefit of pseudo high thermal conductivity for laser powder bed fusion additive manufacturing. Mater. Res. Lett. 2023;11:797–805.
[16] Zeng C, Ding H, Bhandari U, Guo S. Design of crack-free laser additive manufactured Inconel 939 alloy driven by computational thermodynamics method. MRS Commun 2022;12:844–9.
[17] Zeng C, Wen H, Bernard BC, Ding H, Raush JR, Gradl PR, Khonsari M, Guo S. Tensile properties of additively manufactured C-18150 copper alloys. Met Mater Int 2022;28.
[18] Chen Y, Zeng C, Ding H, Emanet S, Gradl PR, Ellis DL, Guo S. Thermophysical properties of additively manufactured (AM) GRCop-42 and GRCop-84. Mater Today Commun 2023;36:106665.
[19] Mertens AI, Delahaye J, Lecomte-Beckers J. Fusion-based additive manufacturing for processing aluminum alloys: state-of-the-art and challenges. Adv Eng Mater 2017;19:1700003.
[20] Bing Z, Shuai L, Xu K-l, Chun X, Wang Z-y, Wang B-j. Hot cracking tendency test and simulation of 7075 semi-solid aluminium alloy. Trans Nonferrous Metals Soc China 2020;30:318–32.
[21] Holzer M, Hofmann K, Mann V, Hugger F, Roth S, Schmidt M. Change of hot cracking susceptibility in welding of high strength aluminum alloy AA 7075. Phys Procedia 2016;83:463–71.
[22] Zeng C, Ghadimi H, Ding H, Nemati S, Garbie A, Raush J, Guo S. Microstructure evolution of Al6061 alloy made by additive friction stir deposition. Materials 2022;15:3676.
[23] Chaudhary B, Jain NK, Murugesan J, Sathiaraj D. Study of microstructure evolution and mechanical properties in friction stir based additive multi-layer manufacturing of Al 6061 alloy: effect of feedstock material form and heat treatment. Mater Today Commun 2023;34:105156.
[24] Tang W, Yang X, Tian C, Xu Y. Interfacial grain structure, texture and tensile behavior of multilayer deformation-based additively manufactured Al 6061 alloy. Mater Char 2023;196:112646.
[25] Ghadimi H, Talachian M, Ding H, Emanet S, Guo S. The effects of layer thickness on the mechanical properties of additive friction stir deposition-fabricated aluminum alloy 6061 parts. Metals 2024;14:101.
[26] Ghadimi H, Ding H, Emanet S, Talachian M, Cox C, Eller M, Guo S. Hardness distribution of Al2050 parts fabricated using additive friction stir deposition. Materials 2023;16:1278.
[27] Yoder JK. Origins of embrittlement of an Al-Zn-Mg-Cu alloy post additive friction stir deposition. Virginia Tech; 2023.
[28] Wells MC. Mechanical and physical properties in additive friction stir deposited aluminum. Virginia Tech; 2022.
[29] Mishra RS, Haridas RS, Agrawal P. Friction stir-based additive manufacturing. Sci Technol Weld Join 2022;27:141–65.
[30] Griffiths RJ, Petersen DT, Garcia D, Yu HZ. Additive friction stir-enabled solid-state additive manufacturing for the repair of 7075 aluminum alloy. Appl Sci 2019;9:3486.
[31] Avery D, Phillips B, Mason C, Palermo M, Williams M, Cleek C, Rodriguez O, Allison P, Jordon J. Influence of grain refinement and microstructure on fatigue behavior for solid-state additively manufactured Al-Zn-Mg-Cu alloy. Metall. Mater. Trans. A. 2020;51:2778–95.
[32] Li Y, Zhang M, Wang H, Lai R, Yang B, Li Y. Microstructure and mechanical properties of Al–Li alloy manufactured by additive friction stir deposition. Mater. Sci. Eng. A. 2023:145753.
[33] Johanson RT. Application of novel additive manufacturing techniques for cost reduction in space launch vehicles. Massachusetts Institute of Technology; 2021.
[34] Hahn GD, Knight KP, Gotawala N, Hang ZY. Additive friction stir deposition of AA7050 achieving forging-like tensile properties. Mater. Sci. Eng. A. 2024;896:146268.
[35] Liu P, Liu F, Wang Y, Zhang Z, Xue P, Wu L, Zhang H, Ni D, Xiao B, Ma Z. Additive manufacturing of commercial Al–Zn–Mg–Cu aluminum alloys with mechanical properties comparable to extruded counterparts. Mater. Sci. Eng. A. 2024;899:146441.
[36] Elshaghoul YG, El-Sayed Seleman MM, Bakkar A, Elnekhaily SA, Albaijan I, Ahmed MM, Abdel-Samad A, Reda R. Additive friction stir deposition of aa7075-T6 alloy: impact of process parameters on the microstructures and properties of the continuously deposited multilayered parts. Appl Sci 2023;13:10255.
[37] Agrawal P, Haridas RS, Yadav S, Thapliyal S, Gaddam S, Verma R, Mishra RS. Processing-structure-property correlation in additive friction stir deposited Ti-6Al-4V alloy from recycled metal chips. Addit Manuf 2021;47:102259.
[38] Martin LP, Luccitti A, Walluk M. Evaluation of additive friction stir deposition of AISI 316L for repairing surface material loss in AISI 4340. J Adv Manuf Technol 2022;121:2365–81.
[39] Mason C, Rodriguez RI, Avery DZ, Phillips BJ, Bernarding BP, Williams M, Cobbs SD, Jordon JB, Allison P. Process-structure-property relations for as-deposited solid-state additively manufactured high-strength aluminum alloy. Addit Manuf 2021;40:101879.
[40] Panigrahi SK, Jayaganthan R. Effect of annealing on thermal stability, precipitate evolution, and mechanical properties of cryorolled Al 7075 alloy. Metall. Mater. Trans. A. 2011;42:3208–17.
[41] Ma K, Wen H, Hu T, Topping TD, Isheim D, Seidman DN, Lavernia EJ, Schoenung JM. Mechanical behavior and strengthening mechanisms in ultrafine grain precipitation-strengthened aluminum alloy. Acta Mater 2014;62:141–55.
[42] Yin X, Deng W, Zou Y, Zhang J. Ultrafine grained Al 7075 alloy fabricated by cryogenic temperature large strain extrusion machining combined with aging treatment. Mater. Sci. Eng. A. 2019;762:138106.
[43] Yin X, Wang W, Wang Z, Guo R, Yu H, Pi Y, Yan W, Wang H, Zhou H. Thermal stability, microstructure evolution and grain growth kinetics of ultrafine grained Al 7075 alloy processed by cryogenic temperature extrusion machining. J Alloys Compd 2023;950:169900.
[44] Kumar SR, Gudimetla K, Venkatachalam P, Ravisankar B, Jayasankar K. Microstructural and mechanical properties of Al 7075 alloy processed by equal channel angular pressing. Mater. Sci. Eng. A. 2012;533:50–4.
[45] Richard D, Adler PN. Calorimetric studies of 7000 series aluminum alloys: I. Matrix precipitate characterization of 7075. Metall Trans A 1977;8:1177–83.
[46] Mohan K, Suresh J, Ramu P, Jayaganthan R. Microstructure and mechanical behavior of Al 7075-T6 subjected to shallow cryogenic treatment. J Mater Eng Perform 2016;25:2185–94.
[47] Hu T, Ma K, Topping T, Schoenung J, Lavernia E. Precipitation phenomena in an ultrafine-grained Al alloy. Acta Mater 2013;61:2163–78.
[48] Flores-Campos R, Mendoza-Ruiz D, Amézaga-Madrid P, Estrada-Guel I, Miki-Yoshida M, Herrera-Ramírez J, Martínez-Sánchez R. Microstructural and mechanical characterization in 7075 aluminum alloy reinforced by silver nanoparticles dispersion. J Alloys Compd 2010;495:394–8.